Nanowire Morphology Control in Sb Metal-derived Antimony Selenide Photocathodes for Solar Water Splitting

Zhenbin Wang, Yongping Gan, Erin Service, Pardis Adams, Thomas Moehl, Wenzhe Niu, S. David Tilley**

Department of Chemistry, University of Zurich, Winterthurerstrasse 190, 8057 Zurich, Switzerland.

Dr. Wenzhe Niu
Laboratory of Photonics and Interfaces, Institute of Chemical Sciences and Engineering, École Polytechnique Fédérale de Lausanne, Lausanne 1015, Switzerland

E-mail: wenzhe.niu@epfl.ch
E-mail: david.tilley@chem.uzh.ch

Keywords: Sb metal, substrate temperature, bilayer structure, nanorods, Sb_2Se_3 photocathodes

We report a facile method to enhance the photoelectrochemical (PEC) performance of Sb_2Se_3 photocathodes by controlling the growth of bilayer Sb_2Se_3 consisting of vertically oriented nanorods on a compact Sb_2Se_3 layer. Sb_2Se_3 thin films with controllable nanorod diameters were achieved by manipulating the substrate temperature during metallic Sb thin film deposition. The lower temperature-derived Sb_2Se_3 photocathode, with a larger nanorod diameter (202 ± 48 nm), demonstrated a photocurrent density of -15.2 mA cm^{-2} at 0 V_{RHE} and an onset potential of 0.21 V_{RHE}. In contrast, the higher temperature-derived Sb_2Se_3 photocathode, with a smaller nanorod diameter (124 ± 28 nm), exhibited an improved photocurrent density of -22.1 mA cm^{-2} at 0 V_{RHE} and an onset potential of 0.31 V_{RHE}. The enhanced PEC performance is attributed to reduced charge recombination facilitated by a shorter charge transport path in the [hk0] direction. This study highlights the significance of morphology control in optimizing Sb_2Se_3 photocathodes, providing insights for future material and device design.

1. Introduction

The carbon dioxide (CO_2) emission produced from fossil fuel combustion has been identified as a primary contributor to global warming. It is urgent to develop efficient methods for generating renewable and clean energy while eliminating CO_2 emissions.[1] Photoelectrochemical (PEC) water splitting is regarded as a promising strategy for converting intermittent sunlight into carbon-free hydrogen fuel.[2,3] In PEC systems, semiconducting materials are employed as photoelectrodes, absorbing photons to generate electron-hole pairs, thereby driving the hydrogen reduction or oxygen oxidation reactions. Over the past few decades, various semiconducting materials have been reported for PEC water splitting, such as silicon (Si),[4] cadmium telluride (CdTe),[5] copper indium gallium selenide (CIGS),[6] Cu-based chalcogenides,[7] cuprous oxide (Cu_2O),[8] bismuth vanadate ($BiVO_4$),[9] and hematite (α-Fe_2O_3).[10] Nonetheless, challenges such as the complex fabrication process of Si, the scarcity of In and Te, the toxicity of Cd, and the poor stability of Cu_2O for the abovementioned materials have severely restricted large-scale commercialization. The development of high-efficiency, low-cost, and stable semiconducting materials used in PEC systems plays a crucial role in meeting the entire society's energy demand.

Antimony selenide (Sb_2Se_3) has received considerable attention as a promising semiconductor material for both photovoltaic (PV) and PEC applications, owing to its low cost, suitable band gap (1.17 eV of direct band gap, and 1.03 eV of indirect band gap), low toxicity, high absorption coefficient ($> 10^5$ cm^{-1}), and high carrier mobility ($\sim$ 10 cm^2 V^{-1} s^{-1}).[11,12] The binary Sb_2Se_3 has only one stable thermodynamic orthorhombic phase, favoring the absence of secondary phases during synthesis. However, the anisotropic property of Sb_2Se_3 results in varying hole mobilities of 1.17, 0.69, and 2.59 cm^2 V^{-1} s^{-1} along the [100], [010], and [001] directions, respectively.[13] Therefore, researchers have devoted significant efforts to optimizing crystal orientation and minimizing defects in Sb_2Se_3 films to enhance performance. Various methods for the preparation of Sb_2Se_3 have been explored in recent years, including thermal evaporation,[14] closed-spaced sublimation,[15] chemical bath deposition,[16] sputtering,[17] spin coating,[18] and vapor transport deposition.[19] Significant progress has been achieved using Sb_2Se_3 absorbers in PV cells and PEC water splitting since 2014. For example, a highly [001]-oriented Sb_2Se_3 photocathode was successfully obtained by extending the selenization time within a sealed quartz tube, delivering a noteworthy photocurrent density of -20.5 mA cm^{-2} at 0 V versus reversible hydrogen electrode (V_{RHE}).[20] Post-annealing treatments were applied to

the Sb_2Se_3 fabrication process to enhance crystallinity.[21,22] Plus, post-selenization was used to address Se deficiency, mitigating bulk defects stemming from Se vacancies and antimony antisites.[23] Zhao *et al.* achieved a record power conversion efficiency of 10.57% in Sb_2Se_3 solar cells by modulating deposition kinetics through the addition of selenourea during the chemical bath deposition process.[16] Furthermore, the Moon group gained impressive progress in the Sb_2Se_3 photocathode through crystal and interface engineering within a short period, resulting in a substantial increase in photocurrent density from -2 mA cm^{-2} to -35 mA cm^{-2} at 0 V_{RHE}, nearly reaching the theoretical maximum photocurrent density (~ 40.9 mA cm^{-2}).[24,25] The Mai group found that controlling substrate temperature during sputtering allowed for the adjustment of the Sb_2Se_3 morphology and orientation.[26]

Inspired by these works, we investigated the impact of metallic Sb properties on the synthesis of Sb_2Se_3 films. Here, we report that the crystal orientation of metallic Sb can be controlled by manipulating the substrate temperature (25 °C and 75 °C) during thermal evaporation. For convenience, we designate the Sb thin films deposited at 25 °C and 75 °C as Sb-L and Sb-H, respectively. Notably, crystal planes with higher surface energy are preferentially exposed when the metallic Sb film is evaporated at higher temperatures. This selective exposure of specific crystal planes significantly influences the morphological evolution of Sb_2Se_3 during the selenization process. Accordingly, we denote the as-prepared Sb_2Se_3 thin films obtained from selenization of Sb-L and Sb-H films as Sb_2Se_3-L and Sb_2Se_3-H, respectively. The photocathode fabricated from Sb_2Se_3-H film, comprising thinner nanorods in the FTO/Au/Sb_2Se_3/TiO_2/Pt configuration, achieves a remarkable photocurrent density of -22.1 mA cm^{-2} at 0 V_{RHE} and an onset potential of 0.31 V_{RHE}. In contrast, the Sb_2Se_3-L photocathode with thicker nanorods only exhibits -15.2 mA cm^{-2} at 0 V_{RHE} and an onset potential of 0.21 V_{RHE}. Moreover, the Sb_2Se_3-H photocathode demonstrates a lower dark current and a superior fill factor compared to the Sb_2Se_3-L photocathode. This straightforward enhancement in PEC performance of the Sb_2Se_3 photocathode, achieved through control of the metallic Sb films, represents a novel approach to synthesizing Sb_2Se_3 films.

2. Results and Discussion

A schematic illustration outlining the synthesis procedure of nanostructured Sb_2Se_3 thin films is depicted in Figure S1. 200 nm of Au layer was deposited onto FTO to form an ohmic contact with the Sb_2Se_3 thin films. Subsequently, the metallic Sb layer was deposited at varying

substrate temperatures using a thermal evaporator. Detailed synthesis information can be found in the experimental section. Both top-view (Figure S2) and cross-sectional scanning electron microscopy (SEM) images (Figure S3) reveal a compact and pinhole-free morphology of metallic Sb thin films. The thickness of both metallic Sb layers is around 240 nm, as determined by profilometer measurement (Figure S3c). X-ray diffraction (XRD) was conducted to determine the effect of substrate temperature on the crystal evolution of metallic Sb thin films. As shown in **Figure 1a**, except for the peaks of Au and FTO, all diffraction peaks of Sb-L and Sb-H match well with the standard diffraction pattern of the rhombohedral Sb phase (PDF No. 85-1324). The relative ratio of surface energies for (003), (102), and (014) planes is 1.91: 2.36: 2.36.[27] This indicates that the Sb-L thin film, dominated by (003) and (006) planes, has lower surface energy than that of the Sb-H thin film. With the increase of the substrate temperature, the (102) and (014) diffraction peaks with higher surface energies become more prominent in the Sb-H thin film.

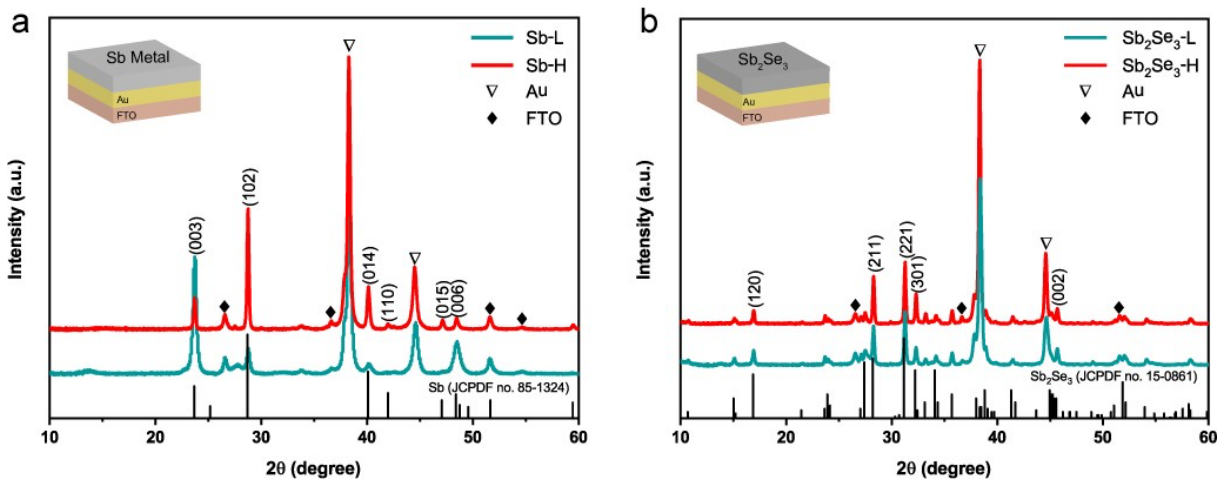

Figure 1. (a) XRD pattern of Sb metal deposited at substrate temperatures of 25 °C and 75 °C. (b) XRD pattern of Sb_2Se_3 synthesized at 325 °C for 30 min by selenizing the corresponding Sb metal sample. The configuration of the samples used for XRD measurement is provided in the inset.

The Sb_2Se_3 thin films were synthesized by subjecting metallic Sb thin films to selenization at 325 °C for 30 min in a sealed tube furnace under Ar protection. Figure 1b displays the XRD pattern of the as-prepared Sb_2Se_3 thin films, which can be well indexed to the standard orthorhombic Sb_2Se_3 phase (JCPDS 15-0861).[28] Apart from the diffraction peaks of FTO and Au, all other peaks belong to the Sb_2Se_3 phase, indicating the formation of a single phase

without secondary phase formation. In addition, both samples display a preferred [hk1] orientation. There is no noticeable difference observed in the XRD patterns between Sb_2Se_3-L and Sb_2Se_3-H thin films, implying that the orientation of metallic Sb films has a negligible impact on the crystallographic orientation of Sb_2Se_3 thin films. Researchers have successfully prepared numerous [hk1]-oriented Sb_2Se_3 thin films through the postselenization of metallic Sb thin films at various temperatures. These Sb thin films, with initially unknown crystal orientations, were produced using diverse methods such as electrodeposition,[29] sputtering,[17] and e-beam evaporation.[30] They found that the crystal orientation evolution of Sb_2Se_3 thin films during postselenization is primarily governed by selenization kinetics rather than the pristine crystal orientation of the Sb thin films. During the selenization process, Se atoms reach the surface of the Sb thin film and rather selenize the surface than diffuse deeper into the Sb film.[31] This results in the formation of $(Sb_4Se_6)_n$ ribbons, allowing continuous selenization along the [001] direction and promoting the perpendicular growth of Sb_2Se_3 films on the substrate. This finding explains the formation of identical crystal orientations in Sb_2Se_3-L and Sb_2Se_3-H thin films, despite the different exposed surfaces of their Sb precursors.

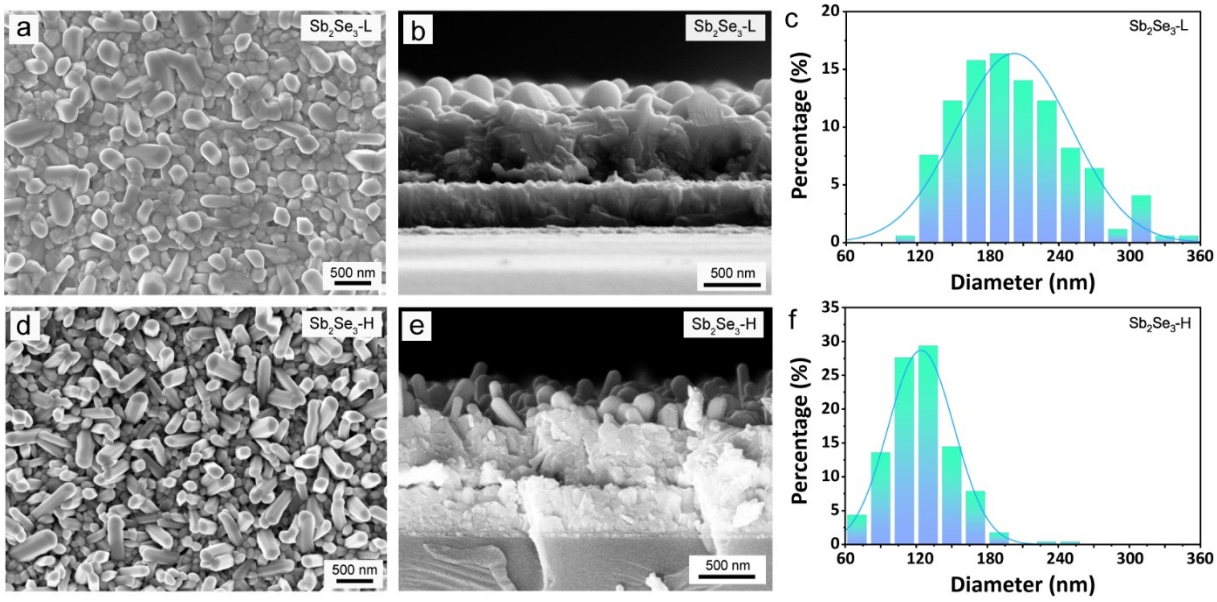

Figure 2. Top-view and cross-sectional SEM images of the (a,b) Sb_2Se_3-L and (d,e) Sb_2Se_3-H thin films. Columnar plots of the characteristic nanorod diameters of the (c) Sb_2Se_3-L and (f) Sb_2Se_3-H thin films.

Nevertheless, the morphology differs between the Sb_2Se_3-L and the Sb_2Se_3-H thin films. **Figure 2** presents the top-view and corresponding cross-sectional SEM images of the Sb_2Se_3-L and Sb_2Se_3-H thin films, indicating the formation of a bilayer structure composed of vertically

oriented nanorods on top of a compact layer in both samples. The thickness of the Sb_2Se_3-L and Sb_2Se_3-H thin films was determined using profilometer measurement (Figure S4), revealing that the thickness of the bottom compact layer for both samples was identical, around 540 nm. The length of vertically oriented nanorods in the Sb_2Se_3-H thin film is longer than that of the Sb_2Se_3-L thin film, which is in good agreement with observations in the cross-sectional SEM images (Figure 2b,e). However, the Sb_2Se_3-H thin film exhibits a denser array of nanorods compared to its counterpart, as evident from the top-view SEM images. For the Sb_2Se_3-L thin film, the diameter of the vertical nanorods is smaller compared with that of the Sb_2Se_3-H thin film. By analyzing more than 200 typical nanorods from the top-view SEM images, the statistical distributions of the diameter of the Sb_2Se_3 nanorods were obtained (Figure 2c,f). The mean diameter values for the Sb_2Se_3-L and Sb_2Se_3-H thin films are 202 ± 48 and 124 ± 28 nm, respectively. Such a considerable difference in the morphology of vertically oriented Sb_2Se_3 nanorods can be attributed to the surface energy-driven growth during the selenization process. The as-deposited metallic Sb-H film, exposing planes with higher surface energies, preferentially reacts with Se atoms to lower their surface energy, forming a thermodynamically stable phase. Therefore, a faster rate of nucleation is expected for the Sb-H thin film, giving rise to more nanorods that are relatively thinner and longer compared to the case with a lower rate of nucleation, where the Sb_2Se_3 has more time to grow laterally (i.e., become thicker) before encountering a neighboring rod.

X-ray photoelectron spectroscopy (XPS) measurements were further carried out to characterize the chemical state of both Sb_2Se_3 thin films. Figure S5 shows XPS spectra of the Sb 3d core levels for the Sb_2Se_3-L and Sb_2Se_3-H surfaces, exhibiting identical results. The binding energies of 529.1 and 538.5 eV associated with $Sb_{5/2}$ and $Sb_{3/2}$ peaks were indexed to the oxidation state of Sb^{3+} in Sb_2Se_3, confirming the formation of Sb_2Se_3. Peaks located at 529.7 and 539.1 eV were attributed to $Sb_{5/2}$ and $Sb_{3/2}$ of Sb_2O_3. A small oxygen peak at 532.2 eV belonging to O 1s further confirmed the existence of Sb_2O_3, which originated from the selenization process due to residual O_2 in the tube.[32] The formation of Sb_2O_3 is more favorable in the presence of O_2 because of the large Gibbs free energy (-605 kJ/mol) and standard molar reaction enthalpy (-718 kJ/mol).[33] Considering that no distinguishable peak from Sb_2O_3 can be observed in the XRD pattern, we assumed that Sb_2O_3 only existed on the film's surface, in accordance with previous literature.[34]

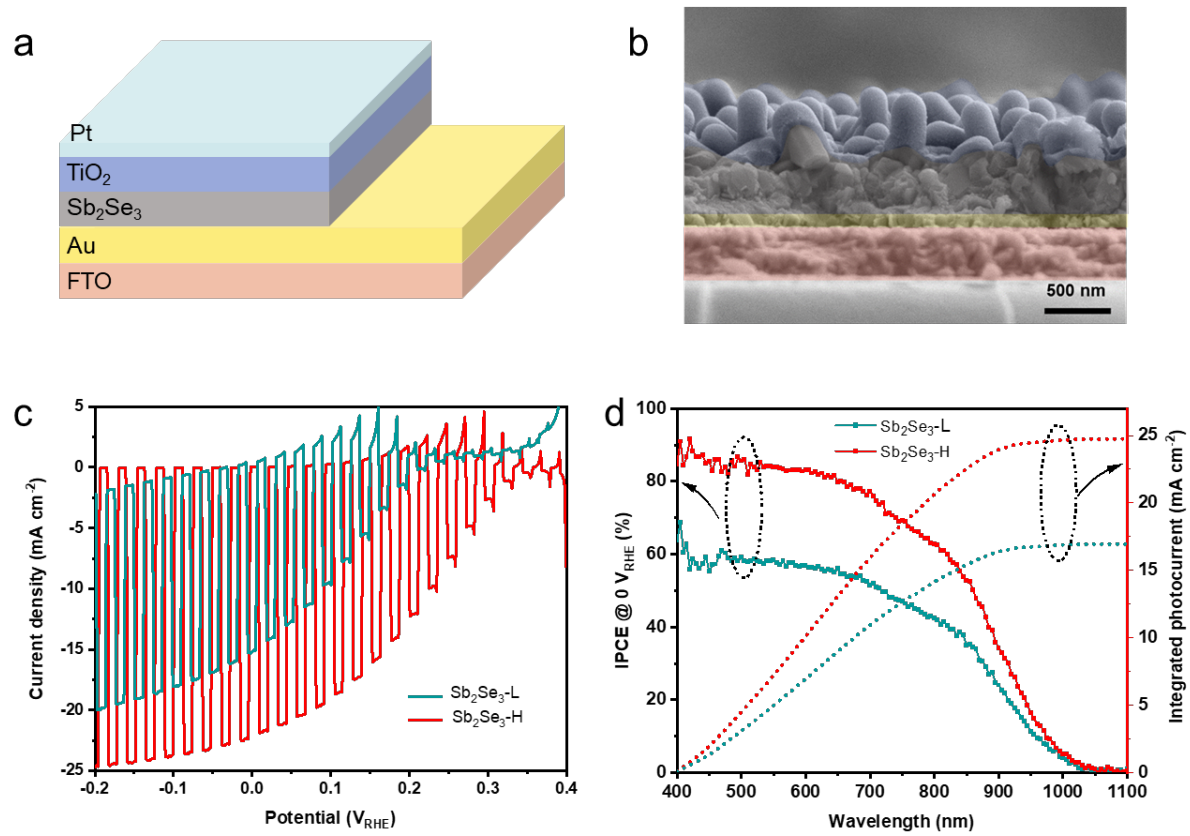

Figure 3. (a) Schematic illustration of the FTO/Au/Sb_2Se_3/TiO_2/Pt device structure. (b) Cross-sectional SEM image of a representative Sb_2Se_3-H device. (c) LSV measurements of the Sb_2Se_3-L and Sb_2Se_3-H photocathodes under intermittent illumination (simulated AM 1.5 G, 100 mW cm^{-2}) in a 1 M H_2SO_4 electrolyte with a scan rate of 10 mV s^{-1}. (d) IPCE and integrated photocurrent of the Sb_2Se_3-L and Sb_2Se_3-H photocathodes biased at 0 V_{RHE} in a 1 M H_2SO_4 electrolyte under 10% white light illumination.

To evaluate the PEC performance of the Sb_2Se_3 photocathodes at the device level, an n-type TiO_2 layer was coated on the surface of the Sb_2Se_3 via atomic layer deposition (ALD), which served as an electron selective contact. A nominal 2 nm Pt layer, acting as a hydrogen evolution catalyst, was deposited by sputtering. The device structure of FTO/Au/Sb_2Se_3/TiO_2/Pt is depicted in **Figure 3a**, and the cross-sectional SEM image of the complete device is shown in Figure 3b. Figure S6 reveals a thin TiO_2 (~ 50 nm) layer uniformly covering both nanostructured Sb_2Se_3 samples, regardless of their nanostructured morphology. The PEC performance of the Sb_2Se_3-L and Sb_2Se_3-H photoelectrodes was measured in a 1 M H_2SO_4 electrolyte (pH 0) under AM 1.5 G simulated illumination (100 mW cm^{-2}), as seen in Figure 3c. The Sb_2Se_3-L photocathode exhibited a photocurrent density of -15.2 mA cm^{-2} at 0 V_{RHE} and an onset potential of 0.21 V_{RHE}. In contrast, the Sb_2Se_3-H photocathode demonstrated a significant enhancement, with a photocurrent density of -22.1 mA cm^{-2} at 0 V_{RHE} and an onset

potential shift to 0.31 V_{RHE}. The Sb_2Se_3-L photocathode exhibited a dark current at negative potentials (< -0.05 V_{RHE}), suggesting the presence of pinholes in the film, whereas no dark current was observed in the Sb_2Se_3-H photocathode. This observation implies that a compact and pinhole-free Sb_2Se_3 film was synthesized by optimizing the metallic Sb film deposition conditions. Additionally, the stability of the Sb_2Se_3-H device was recorded in a 1 M H_2SO_4 solution at 0.2 V_{RHE} shown in Figure S7. The photocurrent density remained at -10 mA cm^{-2} over 2 h and gradually decreased to -8 mA cm^{-2} after running 5 h, retaining 80% of its initial value.

The incident photon-to-current conversion efficiency (IPCE) analysis was performed at 0 V_{RHE} to reveal the light-harvesting capabilities of both Sb_2Se_3 photocathodes in the wavelength range of 400 - 1100 nm, as shown in Figure 3d. The Sb_2Se_3-H photocathode shows an outstanding enhancement in photon-harvesting ability compared to the Sb_2Se_3-L photocathode across the entire spectral region. The IPCE value of the Sb_2Se_3-L photocathode remains below 68%, while the IPCE value of the Sb_2Se_3-H photocathode exceeds 68% across the visible spectrum (400 – 800 nm) and reaches 91% under 420 nm illumination. The integrated photocurrent density for the Sb_2Se_3-L and Sb_2Se_3-H devices, calculated from the IPCE curves using the solar AM 1.5 G spectrum, yields 16.9 mA cm^{-2} and 24.7 mA cm^{-2}, respectively. Both integrated photocurrents agree well with the values determined from LSV measurements. The photocurrent density of the photoelectrode can be analyzed by equation 1,

$$J_{PEC} = J_{abs} \times \eta_{sep} \times \eta_{inj} \quad (1)$$

where J_{PEC} is the measured photocurrent density, J_{abs} is the photon absorption efficiency, η_{sep} is the charge separation efficiency, and η_{inj} is the charge injection efficiency.[35] Figure S8 shows the reflectance and absorbance of both Sb_2Se_3 samples, indicating almost identical photon absorption efficiency. The value of η_{inj} for both Sb_2Se_3 photocathodes can be assumed to be equal due to the same Pt co-catalyst loaded by sputtering. Therefore, we identify that the photocurrent enhancement for the Sb_2Se_3-H photoelectrode derives from the improved η_{sep}, i.e., less recombination occurs in the Sb_2Se_3-H device.

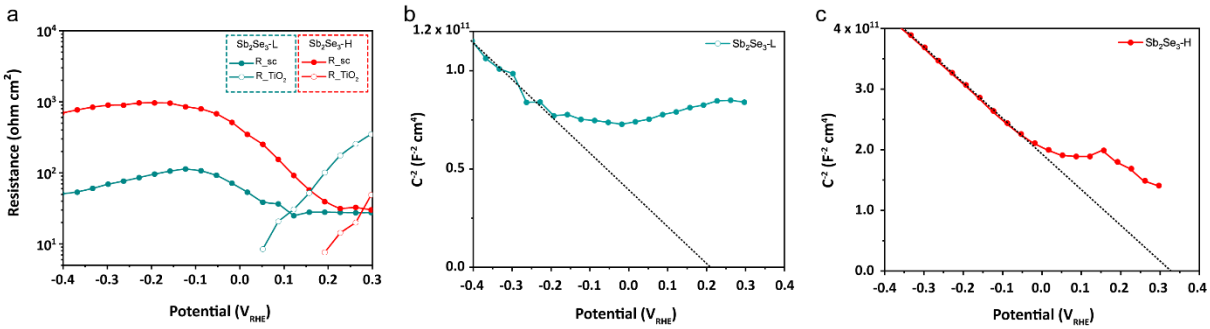

Figure 4. (a) Resistances of the Sb_2Se_3-L and Sb_2Se_3-H photocathodes from the EIS fitting procedure under 10% white light illumination. Mott-Schottky plots of the (b) Sb_2Se_3-L and (c) Sb_2Se_3-H photocathodes obtained from EIS fitting under dark conditions.

Electrochemical impedance spectroscopy (EIS) measurements were conducted to characterize the charge recombination of the Sb_2Se_3 photocathodes. The Nyquist plots of both photocathodes at potentials ranging from 300 to -400 mV_{RHE} are shown in Figure S9. An equivalent circuit (EC) model, consisting of a series resistance and three serially connected RC elements, was employed to fit the Nyquist plot from the EIS measurement, and we identified the RC elements corresponding to the Sb_2Se_3 and TiO_2 layers (see supporting information for details). Our primary focus was on the depletion region at the Sb_2Se_3/TiO_2 interface, as the device structure (FTO/Au/Sb_2Se_3-L, Sb_2Se_3-H/TiO_2/Pt) for both photocathodes is identical except for the Sb_2Se_3 layer. As shown in **Figure 4a**, the R_{SC} of the Sb_2Se_3-H photocathode is one order of magnitude higher than that of the Sb_2Se_3-L photocathode, indicating less recombination of photogenerated electron-hole pairs in the Sb_2Se_3-H photocathode. Mott-Schottky analysis confirms the p-type nature of both Sb_2Se_3-L and Sb_2Se_3-H photocathodes. The Sb_2Se_3-H photocathode shows a slightly more positive flat band potential (0.34 V_{RHE}) compared to the Sb_2Se_3-L photocathode (0.22 V_{RHE}) in Figure 4b and c. Moreover, the resistance at the TiO_2/catalyst interface (R_{TiO2}) decreases and vanishes at 0.05 V_{RHE} for the Sb_2Se_3-L and 0.2 V_{RHE} for the Sb_2Se_3-H as the applied potential approaches the photocurrent onset. The R_{SC} of the Sb_2Se_3-L and Sb_2Se_3 photocathodes starts increasing at 0.1 V_{RHE} and 0.23 V_{RHE}, respectively. These findings align well with the results from LSV measurements, where the Sb_2Se_3-H photocathodes delivered an earlier onset potential.

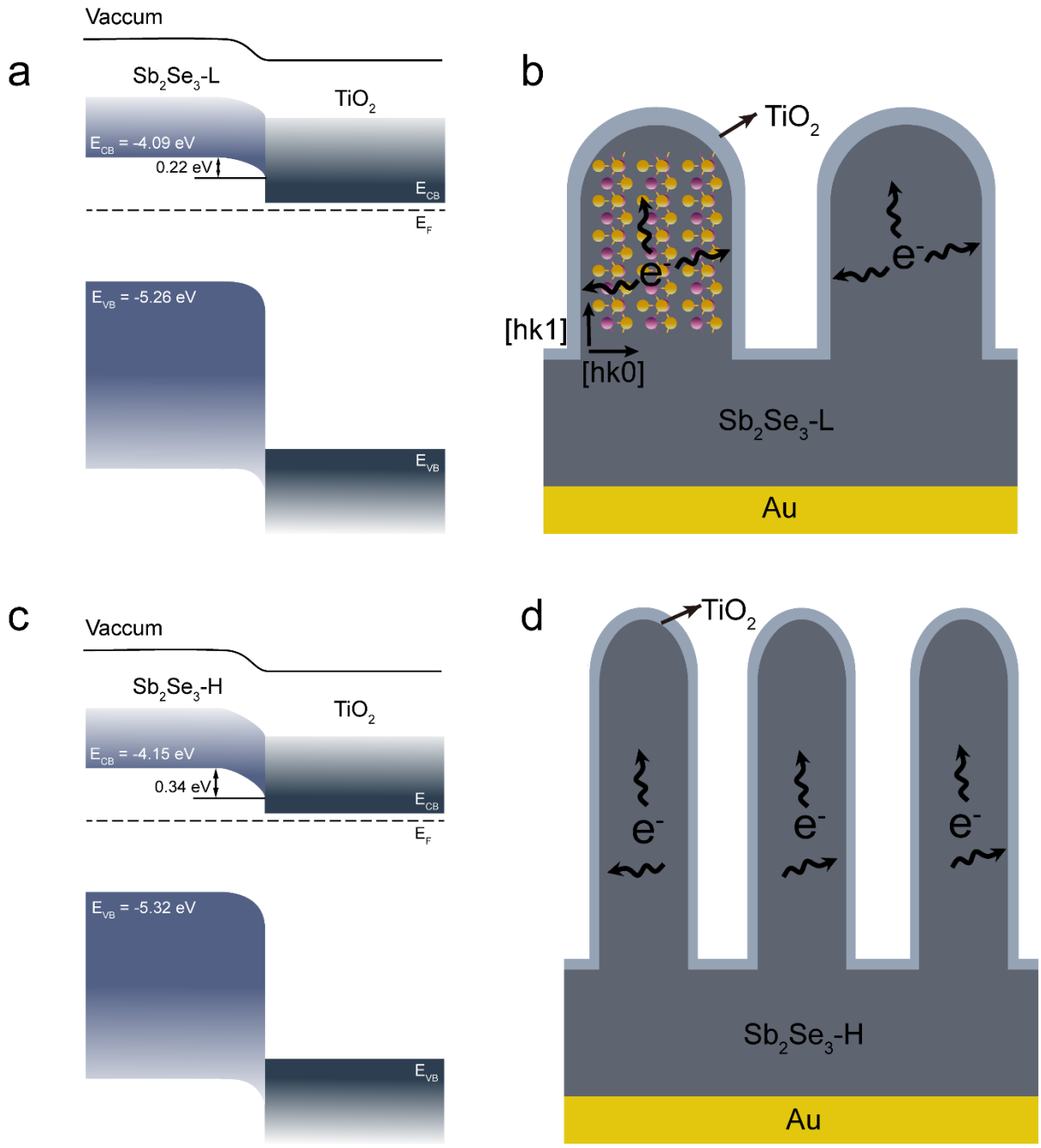

Figure 5. Band diagram of the (a) Sb_2Se_3-L and (c) Sb_2Se_3-H photocathodes. Schematic illustration of the charge separation mechanism in the (b) Sb_2Se_3-L and (d) Sb_2Se_3-H photocathodes.

A hypothesis of the charge separation mechanism was proposed to elucidate the PEC performance enhancement in the Sb_2Se_3-H photoelectrode. Derived from the Tauc plots, the optical band gaps for both Sb_2Se_3 films were determined to be the same (1.17 eV, Figure S10).[36] The Fermi level (E_F) position of both Sb_2Se_3 films can be determined by the flat band potential. The E_F position with respect to the valence band maximum (i.e., the doping level)

was estimated using the XPS valence band maxima (Figure S11). The band gap of TiO_2, taken from the literature, is 3.2 eV.[37] With these values, the energy band alignments of the Sb_2Se_3/TiO_2 heterojunction for both devices were constructed before contact, as seen in Figure S12. The energy band bending of the Sb_2Se_3/TiO_2 heterojunction obtained after E_F equilibration is presented in **Figure 5a,c**. It revealed that a slightly larger band bending formed in the Sb_2Se_3-H photocathode compared with the Sb_2Se_3-L photocathode. This indicates that photoexcited electrons can be more efficiently extracted in the Sb_2Se_3-H photocathode at the same biased potential. In addition, the crystal structure has negligible influence on the PEC performance since both Sb_2Se_3 samples have identical crystal orientations. However, the morphology displays a big difference between the Sb_2Se_3-H and Sb_2Se_3-L samples. For the Sb_2Se_3-H thin film, it has longer and thinner nanorods compared to the Sb_2Se_3-L thin film. Due to the anisotropic properties of Sb_2Se_3, electron mobilities vary, making it easier for photoexcited electrons to transport along $(Sb_4Se_6)_n$ ribbons connected by covalent bonds, while it is more difficult to cross ribbons bonded by van der Waals forces.[13] Based on these morphological differences and the anisotropy in charge carrier mobility, a charge transport mechanism was proposed. The photoexcited electrons in the Sb_2Se_3 bulk must be transported to the TiO_2/electrolyte surface through the nanorods or the valleys among the nanorods where they undergo the hydrogen evolution reaction. When the photoexcited electrons are transported to the vertically oriented nanorods, they can be extracted along either the [hk1] or the [hk0] orientations, as illustrated in Figure 5b, d. The reduced diameter of the nanorods in the Sb_2Se_3-H thin film is advantageous for charge transport due to the decreased charge transport lengths in the [hk0] direction, enhancing the overall PEC performance.

3. Conclusion

We demonstrated a facile method to enhance the PEC performance of Sb_2Se_3 photocathodes by varying the substrate temperature during Sb metal deposition, thereby exposing different Sb surface planes and affecting the resulting Sb_2Se_3 morphology. The Sb_2Se_3-H photocathode exhibited a higher photocurrent density of -22.1 mA cm^{-2} at 0 V_{RHE} and an onset potential of 0.31 V_{RHE}, compared with the Sb_2Se_3-L photocathode, which showed a photocurrent density of -15.2 mA cm^{-2} at 0 V_{RHE} and an onset potential of 0.21 V_{RHE}. The improved PEC performance of the Sb_2Se_3-H photocathode is primarily attributed to the reduced charge recombination and the difference in flat band potential. We proposed that the charge transport mechanism in the thinner vertically oriented nanorods in the Sb_2Se_3-H photocathode facilitate separation and

transport in the horizontal [hk0] direction of the nanorods, thereby enhancing the overall PEC performance.

4. Experimental Section

4.1. Preparation of Sb_2Se_3 Films

Sb powder (99.999 %, Kurt J. Lesker Co. Ltd.) was used as the evaporation source to deposit Sb thin films on FTO/Au substrates via thermal evaporation using the VapourPhase/PicoSphere system (Oxford Vacuum Science Ltd.). Before deposition, FTO glass (FTO TEC 15, Pilkington, Tokyo, Japan) was cleaned sequentially with acetone, a 5% deconex solution in water, distilled water, and isopropanol in an ultrasonic bath for 10 min each, followed by drying under a stream of N_2. After cleaning, a 150 nm Au layer with a 10 nm Cr adhesion layer was deposited by sputtering (Safematic CCU-010 sputter coater). Sb layers (240 nm) were evaporated at substrate temperatures of 25 °C and 75 °C with a deposition rate of 0.1 nm/s under a pressure of 1×10^{-5} Pa. The evaporation source was positioned 35 cm from the sample holder. Subsequently, selenium powder (70 mg) and the as-prepared Sb metal films were placed in separate zones of a two-zone tube furnace (Kejia Co. Ltd.). The Sb metal films were selenized at 325 °C for 30 min with a ramping time of 20 min under Ar protection. Once the process was finished, the tube furnace was opened to cool down to room temperature within 60 min.

4.2. Deposition of TiO_2 Layer and Pt Catalyst

TiO_2 was deposited using atomic layer deposition (ALD) with a Picosun R200 system. The tetrakis (dimenthylamido) titanium (IV) (TDMAT) (99.999 %, Sigma-Aldrich, Buchs, Switzerland), and Milli-Q water were used as the Ti and O precursors, respectively. The titanium precursor was heated to 85 °C, and the reactor chamber was maintained at 120 °C during deposition. For the preparation of Sb_2Se_3 photocathodes, 930 cycles were performed to achieve a 50 nm TiO_2 layer. A small piece of the silicon wafer was placed beside the samples to check the film's thickness by ellipsometry. The Pt cocatalyst was sputtered onto the surface of the as-fabricated Sb_2Se_3/TiO_2 electrodes using a sputter coater (Safematic CCU-010). The distance between the target and the samples was set to 5 cm. The chamber was purged three times before sputtering. A nominal 2 nm Pt layer was sputtered under an applied current of 10 mA for 100 s in an Ar atmosphere.

4.3. Materials Characterization

The morphologies of metallic Sb films and Sb_2Se_3 films were characterized using SEM (Zeiss Gemini 450). XRD (Rigaku SmartLab) with Cu Kα radiation (λ = 0.15406 nm) was employed to characterize the crystal structures of Sb metal and Sb_2Se_3 films. UV-Vis spectra were recorded on a Shimadzu UV-3600 spectrometer in an integrating sphere. The absorbance and reflectance spectra of the Sb_2Se_3 devices were determined, and the bandgaps of the photocathodes were calculated through the Kubelka-Munk function.[38] XPS analysis was conducted using a physical electronics Quantum 2000 X-ray photoelectron spectrometer equipped with monochromatic Al Kα radiation, operating at 15 kV and 32.3 W. To ensure accurate measurements, the instrument's energy scale was calibrated using an Au reference sample. The analysis was performed under a vacuum level of 1×10^{-6} Pa, with an electron take-off angle of 45 degrees and a pass energy of 23.5 eV. Shirley background subtraction was employed with instrument-specific sensitivity factors. Core-level spectra were meticulously deconvoluted to discern contributions from multiple elements, utilizing a GL 30 asymmetric line shape. Notably, a ΔE of 9.34 eV for the Sb 3d doublet was applied for accurate deconvolution of the spectra.

4.4. PEC Performance and EIS Measurements

PEC performance measurements of the Sb_2Se_3 photocathodes were carried out in a typical three-electrode cell configuration, with a Pt wire serving as the counter electrode and an Ag/AgCl electrode (saturated solution of KCl) as the reference electrode. A potentiostat (a Bio-Logic Sp-200) was used to control the potential of the working electrode. The Sb_2Se_3 photocathodes were evaluated in a 1 M H_2SO_4 solution and irradiated with simulated AM 1.5 G illumination from a Xenon lamp, calibrated to 100 mW cm^{-2} with a silicon diode from PV measurements, Inc (PVM558). The area of the photocathode was defined with epoxy resin, and the active area was measured by counting pixels using the freeware image processing software Gimp. IPCE spectra of the Sb_2Se_3 photocathodes were obtained using a home-built system under monochromatic light irradiation at 0 V_{RHE} under 10% white light illumination. The photon flux at each wavelength was first calibrated with a Si photodiode before the measurement of the sample. The IPCE was calculated by the following equation:

$$IPCE(\lambda) = \frac{1240(V \times nm) \times J(mA/cm^2)}{P(mW/cm^2) \times \lambda(nm)} \times 100\% \qquad (2)$$

where J is the photocurrent density, P is the light intensity at each wavelength, λ is the wavelength of the monochromatic light.

4.5. EIS Measurements

EIS measurements were also performed using the same potentiostat combined with a frequency analyzer. A 10% white light illumination from LEDs (SP-12-W5, cool white Luxeon Rebel) was applied for the investigations. The light intensity was calibrated with a calibrated silicon diode with a BK7 window. To minimize the formation and release of gas bubbles, TritonX (1 mM) was added to the H_2SO_4 electrolyte solution. The DC potential ranged from 300 mV to -400 mV_{RHE} and was scanned in 35 mV steps, with a modulation voltage of Vrms = 10 mV. The frequency range applied was 7 MHz to 0.2 Hz, and the EIS spectra were analyzed using ZView software from Scribner.

Acknowledgments

This work was supported by the University of Zurich, the University Research Priority Program (URPP) LightChEC, and the Swiss National Science Foundation (Project # 184737 and Project # 214810). Zhenbin Wang and Yongping Gan thank the China Scholarship Council (CSC) for financial support.

References

[1] W. Wang, M. Xu, X. Xu, W. Zhou, Z. Shao, *Angewandte Chemie International Edition* **2020**, *132*, 140.

[2] C. Jiang, S. J. A. Moniz, A. Wang, T. Zhang, J. Tang, *Chem Soc Rev* **2017**, *46*, 4645.

[3] W. Yang, J. Moon, *ChemSusChem* **2019**, *12*, 1889.

[4] Z. Luo, T. Wang, J. Gong, *Chem Soc Rev* **2019**, *48*, 2158.

[5] J. Su, T. Hisatomi, T. Minegishi, K. Domen, *Angewandte Chemie International Edition* **2020**, *59*, 13800.

[6] T. J. Jacobsson, V. Fjällström, M. Sahlberg, M. Edoff, T. Edvinsson, *Energy Environ Sci* **2013**, *6*, 3676.

[7] B. Chakraborty, R. Beltrán-Suito, V. Hlukhyy, J. Schmidt, P. W. Menezes, M. Driess, *ChemSusChem* **2020**, *13*, 3222.

[8] W. Niu, T. Moehl, P. Adams, X. Zhang, R. Lefèvre, A. M. Cruz, P. Zeng, K. Kunze, W. Yang, S. D. Tilley, *Energy Environ Sci* **2022**, *15*, 2002.

[9] H. S. Han, S. Shin, D. H. Kim, I. J. Park, J. S. Kim, P. S. Huang, J. K. Lee, I. S. Cho, X. Zheng, *Energy Environ Sci* **2018**, *11*, 1299.

[10] S. C. Warren, K. Voïtchovsky, H. Dotan, C. M. Leroy, M. Cornuz, F. Stellacci, C. Hébert, A. Rothschild, M. Grätzel, *Nat Mater* **2013**, *12*, 842.

[11] W. Yang, J. Moon, *ChemSusChem* **2019**, *12*, 1889.

[12] S. Chen, T. Liu, Z. Zheng, M. Ishaq, G. Liang, P. Fan, T. Chen, J. Tang, *Journal of Energy Chemistry* **2022**, *67*, 508.

[13] H. Zhou, M. Feng, K. Song, B. Liao, Y. Wang, R. Liu, X. Gong, D. Zhang, L. Cao, S. Chen, *Nanoscale* **2019**, *11*, 22871.

[14] S. Yao, J. Wang, J. Cheng, L. Fu, F. Xie, Y. Zhang, L. Li, *ACS Appl Mater Interfaces* **2020**, *12*, 24112.

[15] Z. Li, X. Liang, G. Li, H. Liu, H. Zhang, J. Guo, J. Chen, K. Shen, X. San, W. Yu, R. E. I. Schropp, Y. Mai, *Nat Commun* **2019**, *10*, 1.

[16] Y. Zhao, S. Wang, C. Li, B. Che, X. Chen, H. Chen, R. Tang, X. Wang, G. Chen, T. Wang, J. Gong, T. Chen, X. Xiao, J. Li, *Energy Environ Sci* **2022**, *15*, 5118.

[17] G. X. Liang, Y. Di Luo, S. Chen, R. Tang, Z. H. Zheng, X. J. Li, X. S. Liu, Y. K. Liu, Y. F. Li, X. Y. Chen, Z. H. Su, X. H. Zhang, H. L. Ma, P. Fan, *Nano Energy* **2020**, *73*, 104806.

[18] J. Park, W. Yang, J. Tan, H. Lee, J. W. Yun, S. G. Shim, Y. S. Park, J. Moon, *ACS Energy Lett* **2020**, *5*, 136.

[19] Z. Duan, X. Liang, Y. Feng, H. Ma, B. Liang, Y. Wang, S. Luo, S. Wang, R. E. I. Schropp, Y. Mai, Z. Li, *Advanced Materials* **2022**, *34, 2202969*.

[20] H. Zhou, M. Feng, P. Li, X. Gong, D. Zhang, S. Chen, *Sustain Energy Fuels* **2020**, *4*, 3943.

[21] A. Mavlonov, A. Shukurov, F. Raziq, H. Wei, K. Kuchkarov, B. Ergashev, T. Razykov, L. Qiao, *Solar Energy* **2020**, *208*, 451.

[22] L. Zhang, K. Wu, J. Yu, Y. Yu, Y. Wei, *Vacuum* **2021**, *183*, 109840.

[23] G. Liang, M. Chen, M. Ishaq, X. Li, R. Tang, Z. Zheng, Z. Su, P. Fan, X. Zhang, S. Chen, *Advanced Science* **2022**, *9, 2105142*.

[24] J. Kim, W. Yang, Y. Oh, H. Lee, S. Lee, H. Shin, J. Kim, J. Moon, *J Mater Chem A Mater* **2017**, *5*, 2180.

[25] J. Tan, W. Yang, H. Lee, J. Park, K. Kim, O. S. Hutter, L. J. Phillips, S. Shim, J. Yun, Y. Park, J. Lee, J. D. Major, J. Moon, *Appl Catal B* **2021**, *286*, 119890.

[26] K. Shen, Y. Zhang, X. Wang, C. Ou, F. Guo, H. Zhu, C. Liu, Y. Gao, R. E. I. Schropp, Z. Li, X. Liu, Y. Mai, *Advanced Science* **2020**, *7*, 2001013.

[27] L. H. Chou, *J Appl Phys* **1991**, *70*, 4863.

[28] L. Wang, D. B. Li, K. Li, C. Chen, H. X. Deng, L. Gao, Y. Zhao, F. Jiang, L. Li, F. Huang, Y. He, H. Song, G. Niu, J. Tang, *Nat Energy* **2017**, *2*, 1.

[29] R. R. Prabhakar, W. Septina, S. Siol, T. Moehl, R. Wick-Joliat, S. D. Tilley, *J Mater Chem A Mater* **2017**, *5*, 23139.

[30] S. Li, H. Shen, J. Chen, Y. Jiang, L. Sun, A. Raza, Y. Xu, *Journal of Materials Science: Materials in Electronics* **2019**, *30*, 19871.

[31] K. Li, R. Tang, C. Zhu, T. Chen, *Advanced Science* **2024**, *11*.

[32] W. Wang, L. Yao, J. Dong, L. Wu, Z. Cao, L. Hui, G. Chen, J. Luo, Y. Zhang, *Adv Mater Interfaces* **2022**, *9*, 2102464.

[33] X. Liu, J. Chen, M. Luo, M. Leng, Z. Xia, Y. Zhou, S. Qin, D. J. Xue, L. Lv, H. Huang, D. Niu, J. Tang, *ACS Appl Mater Interfaces* **2014**, *6*, 10687.

[34] C. Chen, K. Li, S. Chen, L. Wang, S. Lu, Y. Liu, D. Li, H. Song, J. Tang, *ACS Energy Lett* **2018**, *3*, 2335.

[35] H. Dotan, K. Sivula, M. Grätzel, A. Rothschild, S. C. Warren, *Energy Environ. Sci.* **2011**, *4*, 958.

[36] M. Birkett, W. M. Linhart, J. Stoner, L. J. Phillips, K. Durose, J. Alaria, J. D. Major, R. Kudrawiec, T. D. Veal, *APL Mater* **2018**, *6*, 084901.

[37] R. R. Prabhakar, T. Moehl, S. Siol, J. Suh, S. D. Tilley, *Chemistry of Materials* **2020**, *32*, 7247.

[38] P. Makuła, M. Pacia, W. Macyk, *Journal of Physical Chemistry Letters* **2018**, *9*, 6814.

Table of Contents

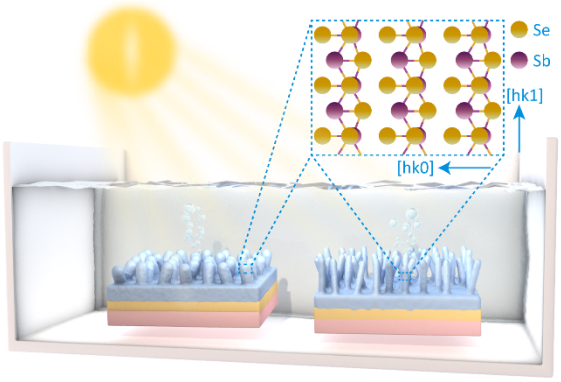

We present a facile method to enhance the PEC performance of the Sb_2Se_3 photocathodes by varying substrate temperatures during Sb metal deposition. Thinner nanorods translate to higher photocurrents due to reduced charge recombination resulting from minimizing charge transport in the hk0 direction.

Supporting information

Nanowire Morphology Control in Sb Metal-derived Antimony Selenide Photocathodes for Solar Water Splitting

Zhenbin Wang, Yongping Gan, Dr. Erin Service, Dr. Pardis Adams, Dr. Thomas Moehl, Dr. Wenzhe Niu*, Prof. Dr. S. David Tilley*

E-mail: wenzhe.niu@epfl.ch
E-mail: david.tilley@chem.uzh.ch

Department of Chemistry, University of Zurich, Winterthurerstrasse 190, 8057 Zurich, Switzerland.

Dr. Wenzhe Niu
Laboratory of Photonics and Interfaces, Institute of Chemical Sciences and Engineering, École Polytechnique Fédérale de Lausanne, Lausanne 1015, Switzerland

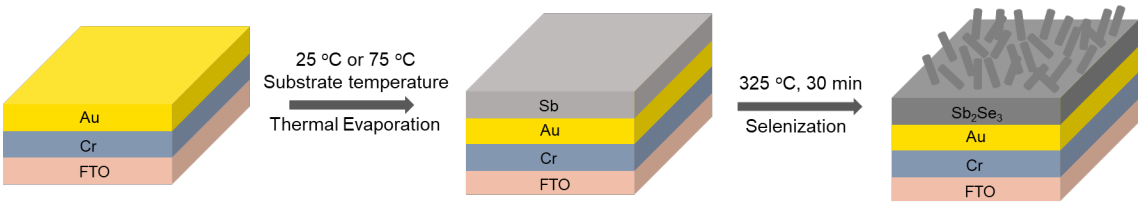

Figure S1. Schematic illustration showing the fabrication process of the nanostructured Sb_2Se_3 thin films.

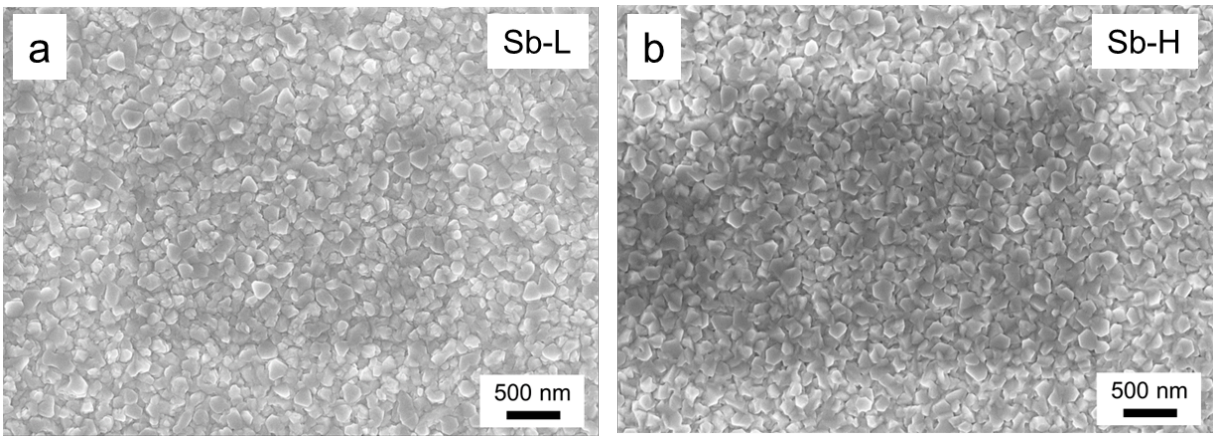

Figure S2. Top-view SEM images of the (a) Sb-L and (b) Sb-H thin films evaporated at substrate temperatures of 25 °C and 75 °C.

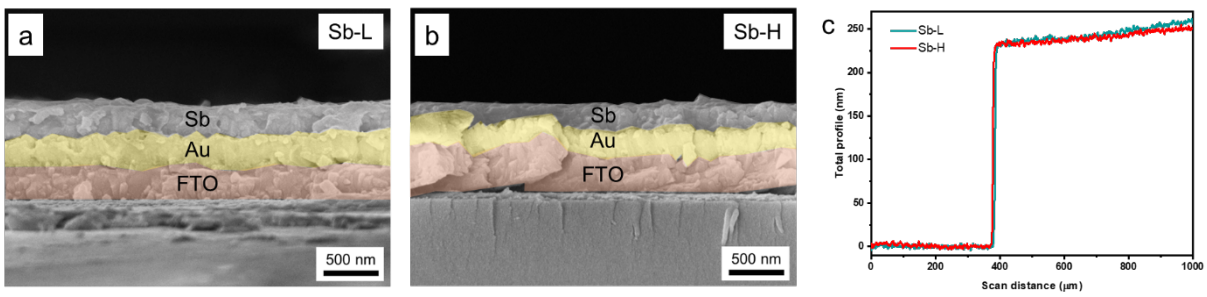

Figure S3. Cross-sectional SEM images of the (a) Sb-L and (b) Sb-H thin films. (c) The thickness of the metallic Sb thin films determined by a profilometer.

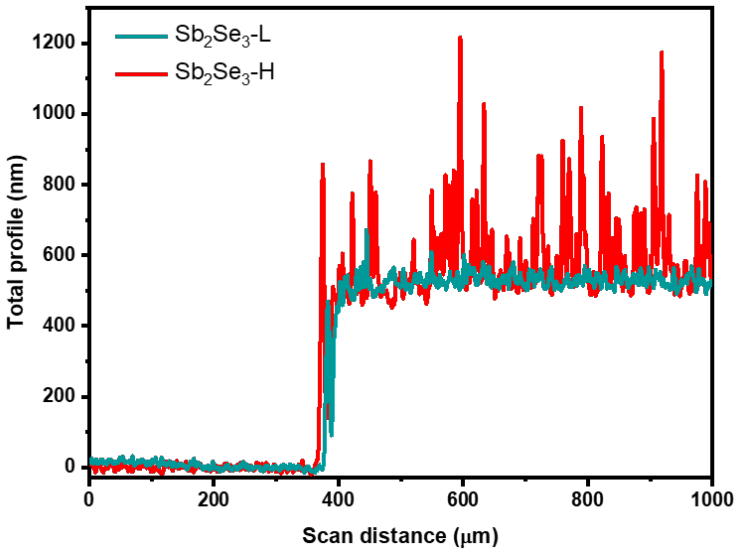

Figure S4. The thickness of the Sb_2Se_3 thin films determined by a profilometer.

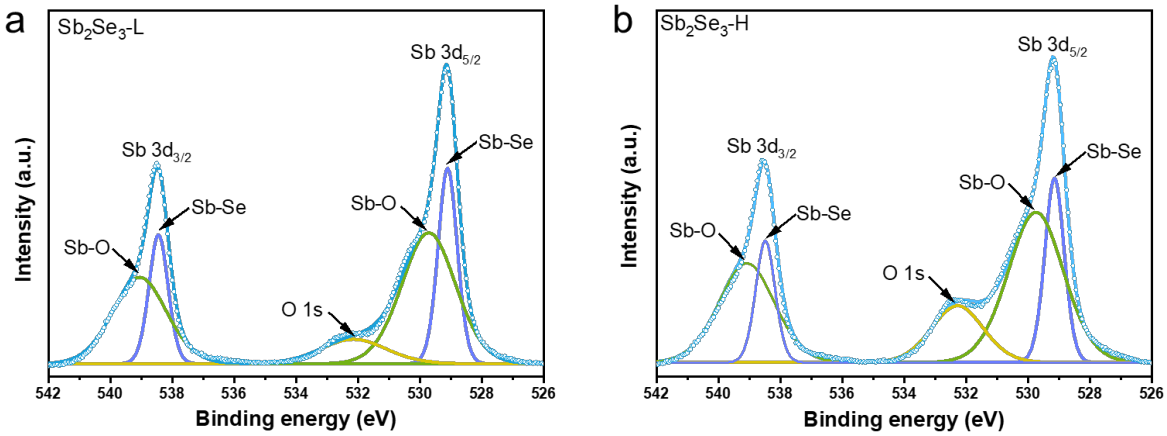

Figure S5. Sb 3d XPS spectra of (a) the Sb_2Se_3-L and (b) Sb_2Se_3-H thin films.

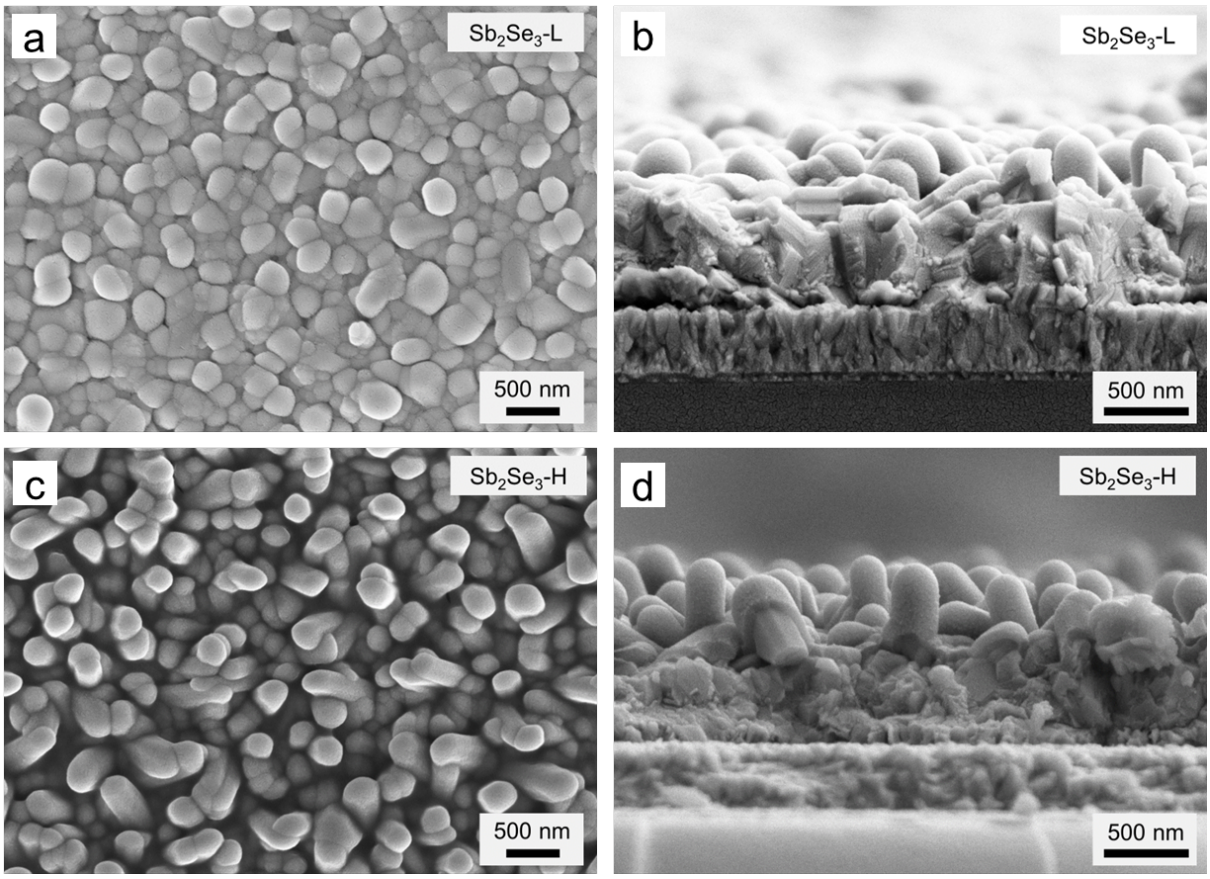

Figure S6. Top-view and cross-sectional SEM images of the (a, b) FTO/Au/Sb_2Se_3-L/TiO_2/Pt and (c, d) FTO/Au/Sb_2Se_3-H/TiO_2/Pt thin films.

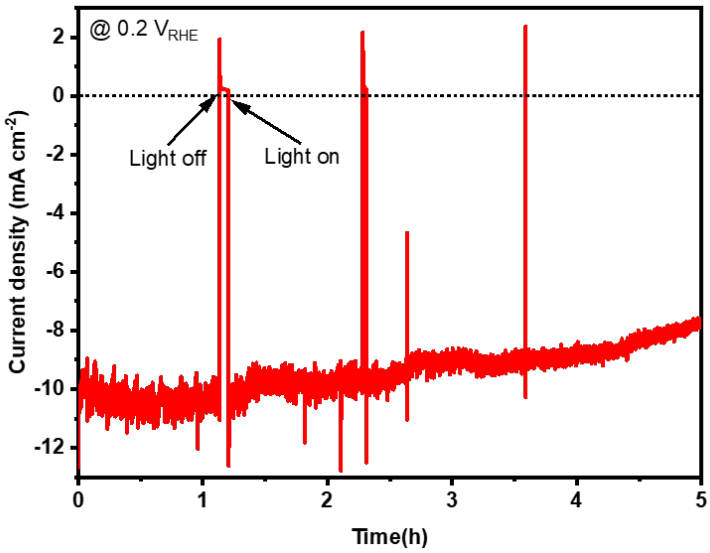

Figure S7. Stability test of the Sb_2Se_3-H photocathode at 0.2 V_{RHE} under AM 1.5 G simulated solar illumination (100 mW cm^{-2}) in a 1 M H_2SO_4 electrolyte solution.

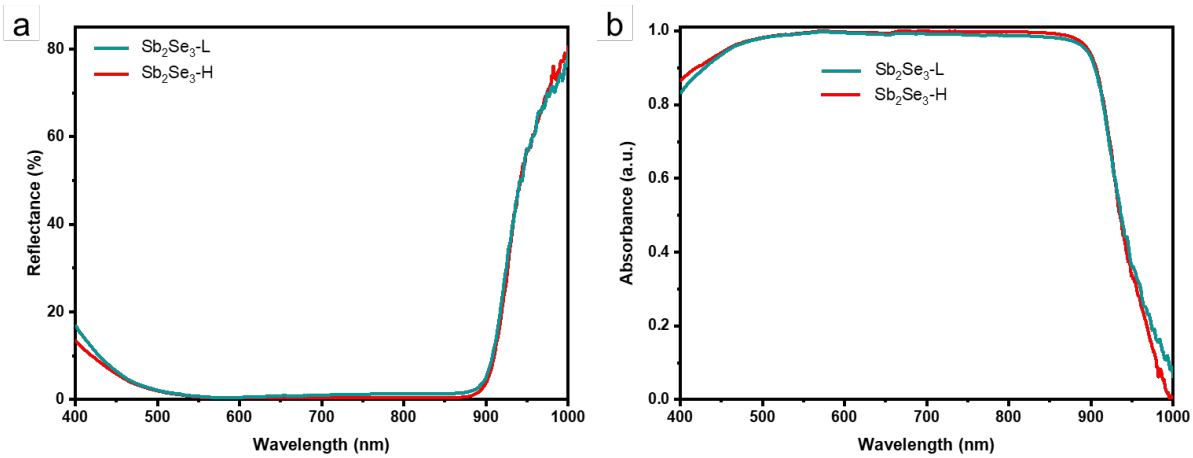

Figure S8. (a) The reflectance spectrum of the FTO/Au/Sb_2Se_3-L/TiO_2/Pt and FTO/Au/Sb_2Se_3-H/TiO_2/Pt devices. (b) The absorbance spectrum of the FTO/Sb_2Se_3-L/TiO_2/Pt and FTO/Sb_2Se_3-H/TiO_2/Pt devices.

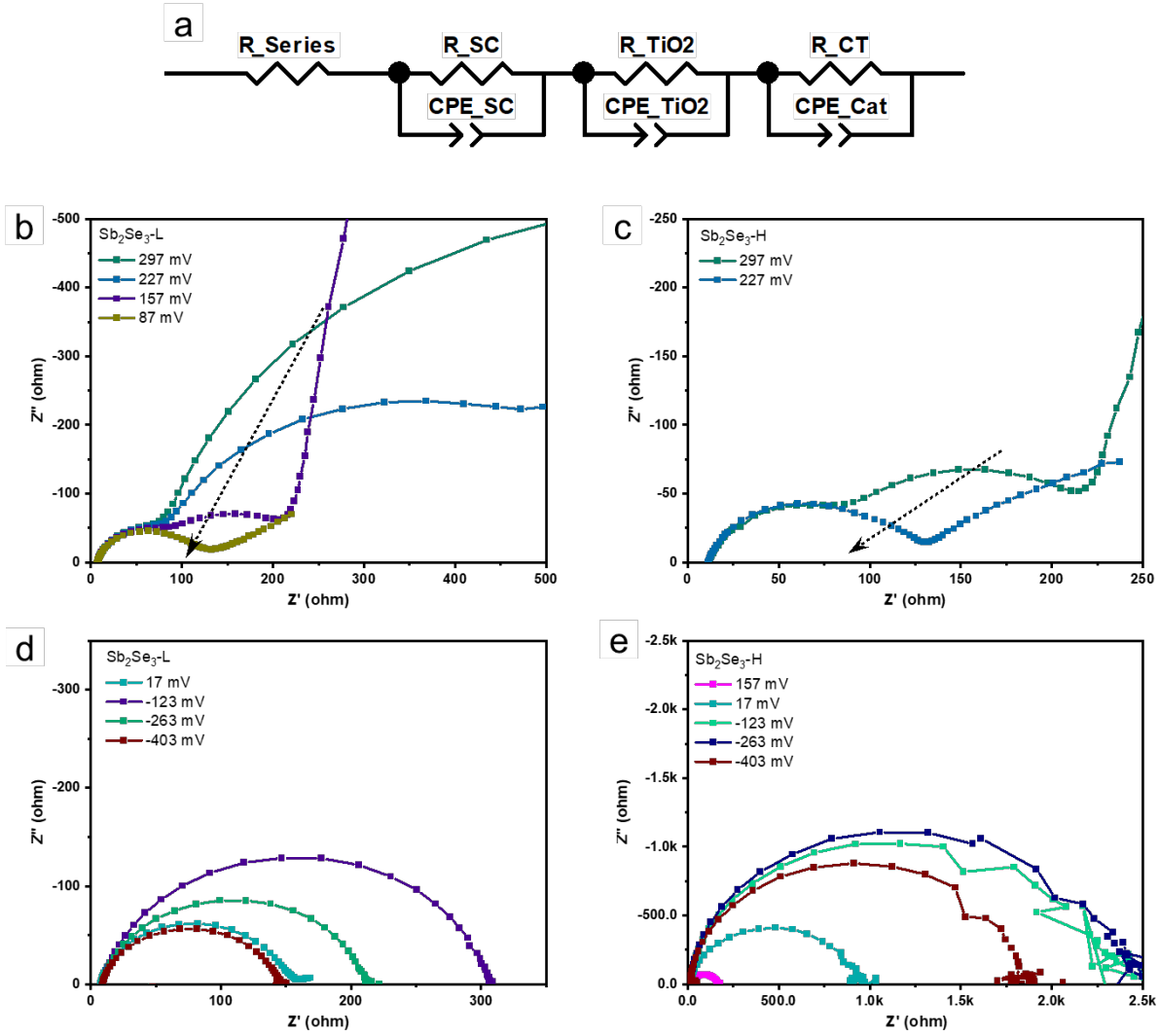

Figure S9. (a) The equivalent circuit is used for the EIS fitting. Nyquist plots of (b) the Sb_2Se_3-L and (c) Sb_2Se_3-H photocathodes before onset potential under 10% white light illumination. Nyquist plots of (d) the Sb_2Se_3-L and (e) Sb_2Se_3-H photocathodes after onset potentials under 10% white light illumination.

The Nyquist plots at different applied potentials are shown in Figure S9. The equivalent circuit model (Figure S9a) was used for the EIS fitting. To improve the fitting accuracy, a constant phase element (CPE) was utilized instead of an ideal capacitor. The Nyquist plots at different applied potentials are shown in Figure S9. The equivalent circuit model (Figure S9a) was used for the EIS fitting. To improve the fitting accuracy, a constant phase element (CPE) was utilized instead of an ideal capacitor. At potentials positive of photocurrent onset, three elements are observed (Figure S9b,c): a high-frequency element corresponding to the semiconductor, a mid-frequency element corresponding to the TiO_2, and a low frequency element corresponding to the catalyst. The resistances corresponding to the TiO_2 and catalyst decrease as the potential

moves towards more negative values. As the onset potential is reached, they then become negligible, indicating that thermodynamic barriers to photogenerated charge transfer have been overcome. After the onset potential, only the element corresponding to the semiconductor remains. This element increases in size, such that the capacitance corresponds to the space charge capacitance, and the resistance corresponds to the inverse slope of the JV curve at that potential (the DC resistance).

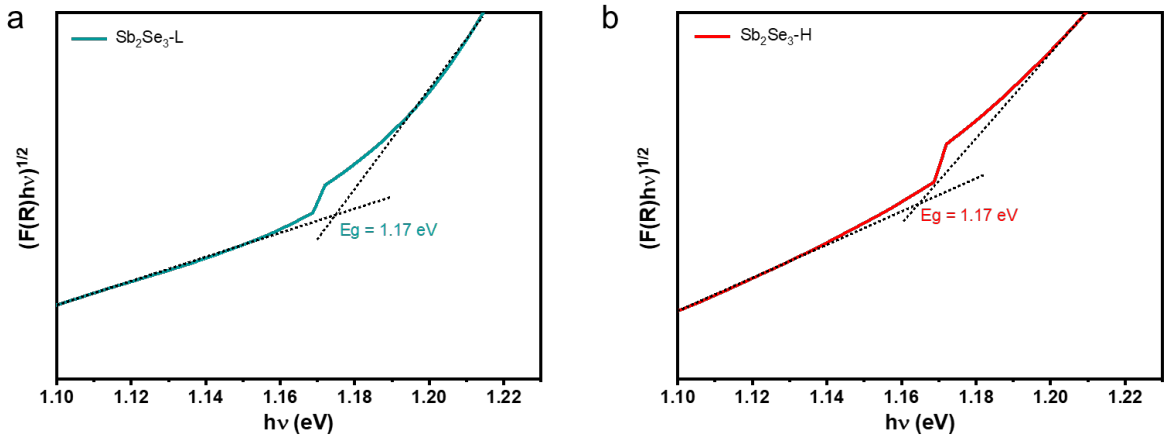

Figure S10. The bandgap of the Sb_2Se_3-L and Sb_2Se_3-H samples determined via the Kubelka-Munk function.

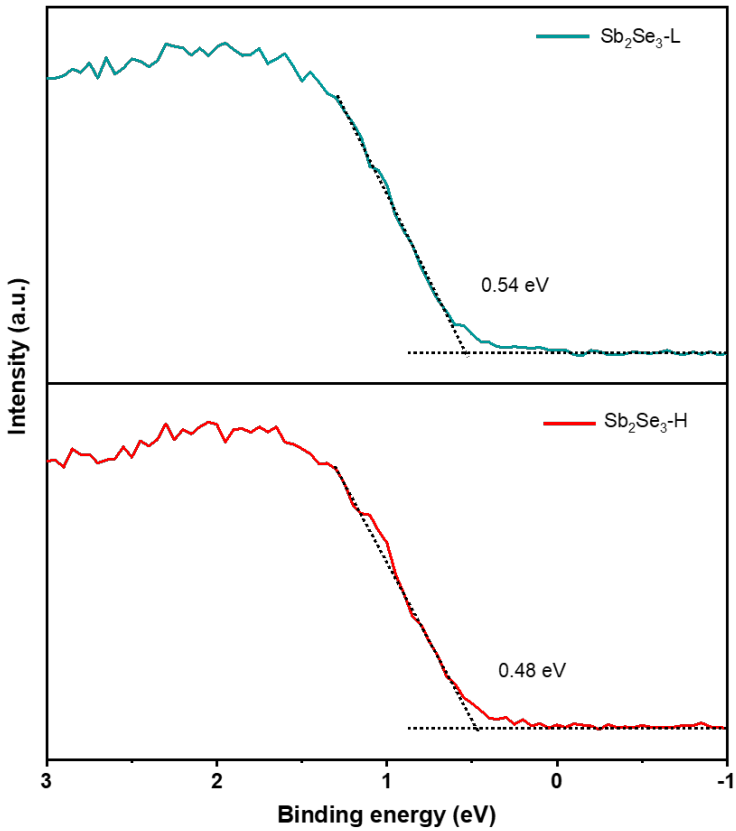

Figure S11. XPS measurements of the valence band edge of Sb_2Se_3-L and Sb_2Se_3-H thin films.

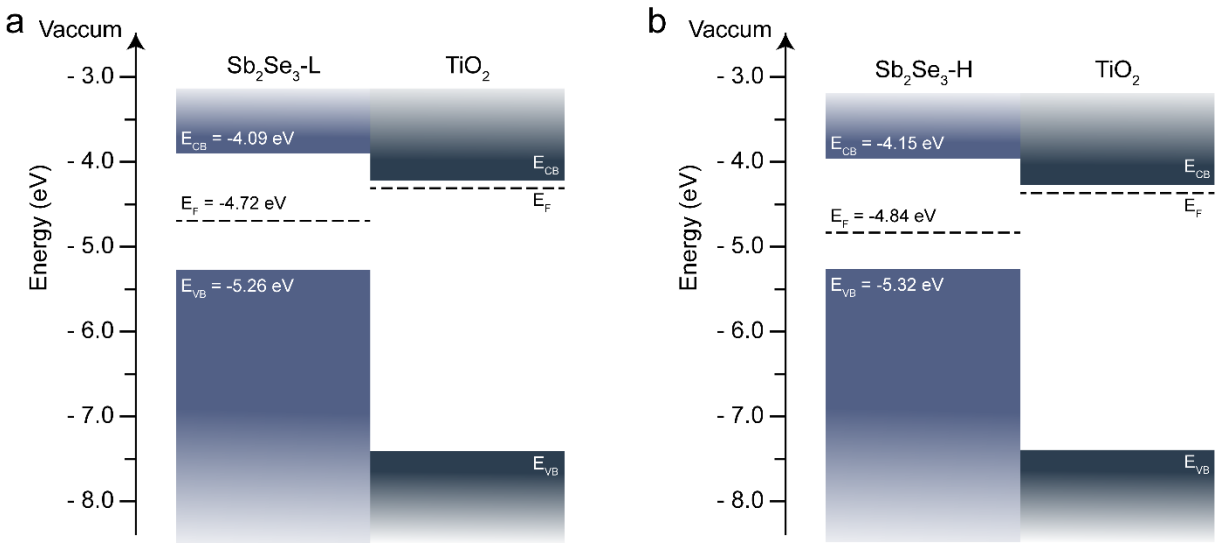

Figure S12. (a) Band alignments of the (a) Sb_2Se_3-L/TiO_2 and (c) Sb_2Se_3-H/TiO_2 devices.

The bandgaps of the Sb_2Se_3-L and Sb_2Se_3-H devices were determined to be 1.17 eV using the Kubelka-Munk function. The Fermi level (E_F) positions of both devices with respect to the vacuum level were determined by the flat band potential. The flat band potentials obtained from Mott-Schottky plots indicate the difference between the Fermi levels of Sb_2Se_3 and the redox potential of the H_2SO_4 electrolyte solution (pH 0, $E_{H+/H2}$, 0 V_{RHE}). The work functions of Sb_2Se_3-L and Sb_2Se_3-H were calculated to yield values of 4.72 V and 4.84 V, respectively. XPS measurements revealed energetic distances from the E_F to the valence band maximum (VBM) of 0.54 eV for Sb_2Se_3-L and 0.48 eV for Sb_2Se_3-H. Based on these measurements, the VBM positions were determined to be 5.26 eV for Sb_2Se_3-L and 5.32 eV for Sb_2Se_3-H, while the conduction band minimum (CBM) positions were calculated to be 4.09 eV for Sb_2Se_3-L and 4.15 eV for Sb_2Se_3-H. According to this, the band alignments of the Sb_2Se_3-L/TiO_2 and Sb_2Se_3-H/TiO_2 interfaces were constructed.